Basal crevasse formation on Byrd Glacier, East Antarctica, as proxy for past subglacial flooding events

Sarah F Child[1], Leigh A Stearns[2], Cornelis J. van der Veen[2], and Pedro Elosegui[3]

[1]University of Colorado
[2]University of Kansas
[3]MIT

November 21, 2022

Abstract

Linear elastic fracture mechanics (LEFM) suggests that short-lived flow accelerations, such as the one observed in the 2006 Byrd Glacier, East Antarctica, subglacial flooding event, can initiate abnormally large basal crevasses at the grounding line. Airborne radar measurements acquired in 2011 reveal hundreds of basal crevasses ranging in height ˜40—335 m. Particle tracking results show that the formation of the largest basal crevasse occurred at the grounding line during the 2006 flooding event. Very large basal crevasses form distinctive surface depressions directly overhead, which are observed along the Byrd Glacier flowline to the terminus of the Ross Ice Shelf. By using these surface depressions as proxy for abnormally large basal crevasses, we create a timeline of past subglacial flooding events on Byrd Glacier. Understanding the frequency of flooding events and their effect on glacier dynamics will help inform subglacial hydrology models and models of ice sheet stability.

Basal crevasse formation on Byrd Glacier, East Antarctica, as proxy for past subglacial flooding events

Sarah F. Child[1,2], Leigh A. Stearns[1,3], C. J. van der Veen[4], Pedro Elósegui[5,6]

[1]Department of Geology, University of Kansas, Lawrence, KS 66045, USA
[2]Cooperative Institute for Research in Environmental Sciences, University of Colorado, Boulder, CO 80309, USA
[3]Center for Remote Sensing of Ice Sheets, University of Kansas, Lawrence, KS 66045, USA
[4]Department of Geography & Atmospheric Sciences, University of Kansas, Lawrence, KS 66045, USA
[5]Massachusetts Institute of Technology, Haystack Observatory, Westford, MA, 01886 USA
[6]Institute of Marine Sciences, ICM-CSIC, Barcelona, Spain

Key Points:

- Increased tensile stress from subglacial flooding may initiate abnormally large basal fractures.
- We date abnormally large basal crevasses via feature tracking of overlying surface depressions.
- These rapid changes in glacier dynamics appear to have no effect on Byrd Glacier's stability.

Corresponding author: Sarah F. Child, sarah.child@colorado.edu

Abstract

Linear elastic fracture mechanics (LEFM) suggests that short-lived flow accelerations, such as the one observed in the 2006 Byrd Glacier, East Antarctica, subglacial flooding event, can initiate abnormally large basal crevasses at the grounding line. Airborne radar measurements acquired in 2011 reveal hundreds of basal crevasses ranging in height ∼40 – 335 m. Particle tracking results show that the formation of the largest basal crevasse occurred at the grounding line during the 2006 flooding event. Very large basal crevasses form distinctive surface depressions directly overhead, which are observed along the Byrd Glacier flowline to the terminus of the Ross Ice Shelf. By using these surface depressions as proxies for abnormally large basal crevasses, we create a timeline of past subglacial flooding events on Byrd Glacier. Understanding the frequency of flooding events and their effect on glacier dynamics will help inform subglacial hydrology models and models of ice sheet stability.

Plain Language Summary

Flooding events that occur under the Antarctic Ice Sheet are difficult to observe due to their location and a limited supply of remotely sensed data. In 2006, a flooding event occurred at Byrd Glacier that was followed by a ∼10% increase in the glacier's speed. At approximately the same time as the flood, an abnormally large basal crevasse formed within Byrd Glacier's grounding zone. Without monthly satellite data, we cannot be certain exactly when the speedup began and ended, but modeling results using the velocity data that we do have from December 2005 to February 2007 shows that significantly larger basal crevasses initiate during these speedups due to an increase in extensional stresses. These abnormally large basal crevasses form surface depressions directly overhead, which are observable from satellite data. We hypothesize that all surface depressions overlie abnormally large basal crevasses whose initiations are the result of speedups caused by subglacial flooding events. We use the surface depressions as proxies for past subglacial flooding events to better understand subglacial hydrology and its relationship with glacier dynamics.

1 Introduction

Basal crevasses are common on Antarctic ice shelves. They form when tensile stress and water pressure, which act to widen the crevasse, exceed lithostatic stress, which acts to close it (Rist et al., 1996, 2002; Van der Veen, 1998). Basal crevasses seem to form exclusively at glacier grounding lines, then advect down-flow through the ice shelf, often providing zones of weakness at which icebergs detach (Jezek, 1984; Luckman et al., 2012).

The location and geometry of basal crevasses can be mapped with ground-based or airborne radar measurements (Jezek et al., 1979; Jezek & Bentley, 1983; McGrath et al., 2012; Luckman et al., 2012; Vaughan et al., 2012). Along the Byrd Glacier flowline, radar data show that basal crevasses are neither uniformly sized nor spaced. Crevassing that does not occur at regular time intervals is the result of short-term variations in the stresses modulating crevasse initiation. Of the modulating stresses, tensile stress is the only variable that undergoes short-term variations, as exhibited by changes in ice velocity.

In this study, we investigate the formation and evolution of basal crevasses extending from the Byrd Glacier grounding line onto the Ross Ice Shelf (RIS) (Figure 1A). We identify over 300 basal crevasses within ∼5 km of the grounding line. Of the crevasses whose heights we are able to measure, 86% are shorter than 100 m, but a few crevasses, including the one closest to the grounding line, exceed 300 m in height. We hypothesize that the rapid drainage of two subglacial lakes in the Byrd Glacier catchment (Stearns

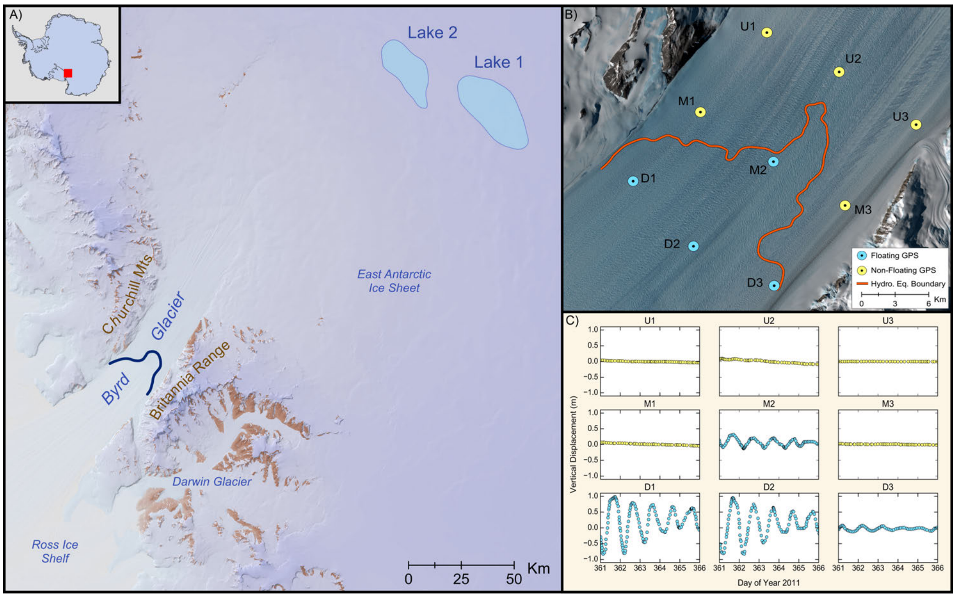

Figure 1. A) Map of Byrd Glacier and the subglacial lakes located ~175 km up-flow from the grounding line (Stearns et al., 2008). The trunk of Byrd Glacier is ~25 km wide and ~100 km long; ice flow is from the top right to the bottom left. The background image is a hillshade made from the Polar Geospatial Center's Regional Elevation Model of Antarctica 8 m mosaics. The grounding line, derived in section 3.1, is shown as the navy blue line. The extent of (A) is outlined in red on the inset map at the upper left-hand corner. B) The grounding zone is between the limit of tidal flexure (just down-flow of yellow GPS points) and hydrostatic equilibrium (orange line). GPS labels represent up-flow (U), middle (M), and down-flow (D). C) Time-varying estimates of the vertical component of site position of the nine GPS receiving systems that straddle the grounding line, for six days in December 2011.

et al., 2008; Carter et al., 2017) led to the formation of this anomalously large basal crevasse at the grounding line. And, because large basal crevasses cause surface depressions, we explore whether the train of surface depressions between Byrd Glacier and the calving front of the Ross Ice Shelf can be used as proxies for past subglacial flooding events.

2 Data and Methods

2.1 Grounding line location

Basal crevasses appear to only form at the grounding line, where tensile stresses and water pressure can exceed the lithostatic stress (Jezek & Bentley, 1983; Bentley, 1987). The grounding line is located within a grounding zone (Figure 1), estimated through tidal flexure (up-flow limit, where a glacier undergoes vertical displacement due to ocean tides) and the hydrostatic equilibrium boundary (down-flow limit, where a glacier is fully floating) (Vaughan, 1994; Fricker & Padman, 2006; Brunt et al., 2010). We use both *in situ* GPS observations and airborne and satellite data to identify these limits (see supplemental for more information).

2.2 Basal crevasse geometry

2.2.1 Observed crevasse locations and heights

From December 2011 to January 2012, the Center for Remote Sensing of Ice Sheets (CReSIS) collected a dense grid of airborne radar data over Byrd Glacier. In this study, we only use the data recorded by the radar depth sounder (MCoRDS V2) operating at 180-210 MHz (Gogineni et al., 2014). The main sources of error for MCoRDS V2 are multiple reflectors, electronic noise, and off-nadir reflections (CReSIS, 2014), which is an estimated error of ∼30.6 m in thickness measurements (Gogineni et al., 2014). The elevations are referenced to the WGS84 ellipsoid.

We ascertain locations and heights of the basal crevasses directly from the MCoRDS V2 echograms. Basal crevasses open in the same direction as the radar flight appear as hyperbola in radar echograms and the apex of those hyperbola represents the peak of the fracture. Crevasse heights are estimated by identifying the apex and both asymptotes of a hyperbola. In some cases, basal crevasses are so numerous that the asymptotes of neighboring hyperbola intersect and estimating crevasse height is not possible. We only report crevasse heights where both asymptotes are clearly identifiable.

2.2.2 Modeled crevasse locations and heights

CReSIS radar data were not collected coincident with the subglacial flooding event in 2006. To determine whether conditions during flooding events could produce abnormally large basal crevasses, we model crevasse heights using linear elastic fracture mechanics (LEFM) with flood and non-flood parameters (see supplemental for more information). LEFM calculates a stress intensity factor (K_I); when this stress intensity factor exceeds the fracture criterion, or ice toughness, then a crack will propagate (Rist et al., 1996; Van der Veen, 1998), following:

$$K_I = \int_0^{h_0} \frac{2\theta_n(z)}{\sqrt{\pi h}} G(\gamma, \lambda) dz. \tag{1}$$

Here, h_0 is the size of the starter crack, which we set to 2 m after Rist et al. (2002) and a value of .155 $MPa\ m^{\frac{1}{2}}$ for K_I (Rist et al., 1999). $G(\gamma, \lambda)$ is a function of $\lambda = \frac{h}{H}$ and $\gamma = \frac{z}{h}$, established from fitting a polynomial curve to the modelled stress intensity values, with H the ice thickness and z the depth within the glacier (Van der Veen, 1998). $\theta_n(z)$ represents the combined stresses (tensile, lithostatic, and water pressure) acting at the crevasse tip. Tensile stress is calculated from strain rates, following Glen's Flow Law, and using a rate factor appropriate for surface ice at -20°C (after Van der Veen et al. (2014)). Strain rates were determined from velocity data collected in February 1989 to January 1990 and December 2005 to February 2007 (Stearns et al., 2008).

2.2.3 Surface depressions

Ice overlaying a large basal crevasse adjusts to hydrostatic equilibrium by forming a surface depression (Shabtaie & Bentley, 1982; Luckman et al., 2012). Several radar studies describe the relationship between surface depressions and basal crevasses (Jezek et al., 1979; Luckman et al., 2012; McGrath et al., 2012; Humbert et al., 2015). On Byrd Glacier, anomalously large basal crevasses have overlying surface depressions which are detectable from radar echograms and optical satellite imagery (see Figure 2). We use the panchromatic band from Landsat 8 OLI imagery collected in January 2016 – December 2017 to identify surface depressions.

We determine the age of the surface depressions by using a particle tracking algorithm (after Konikow and Bredehoeft (1978)) from the depressions' centroid locations

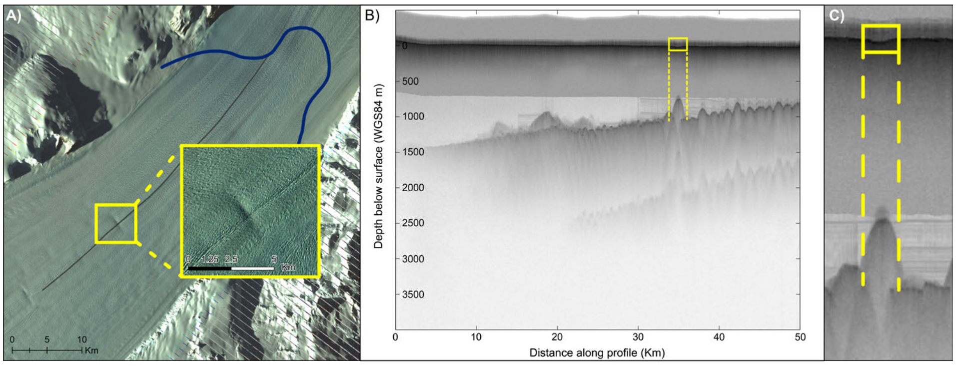

Figure 2. A). The surface depression overlaying a large ∼290 m tall basal crevasse (shown in panels (B) and (C)) with the CReSIS flight line in gray. The background is a Landsat 7 ETM+ image (Bands 2,3,4) acquired on February 22, 2011, approximately 10 months before CReSIS data were collected. B). Along-flow, vertical cross-section CReSIS echogram (ID: 20111205_08_003) highlighting the ∼290 m tall crevasse in yellow. C). Zoomed-in view of the ∼290 m crevasse and the overlying surface depression.

to the grounding line. This approach allows us to determine the flow path of each depression and an estimate of when the crevasse formed at the grounding line. Byrd Glacier has a lack of merging flow bands from the grounding line to the ice shelf terminus, which suggests the glacier has maintained a consistent flow regime for the last few centuries (Hulbe & Fahnestock, 2007; LeDoux et al., 2017). The little to no deviation in Byrd Glacier's temporal speeds and stress regime means that accurate estimates of basal crevasse flow advection can be determined from present-day velocity and ice flow data. The velocity data used for particle tracking is from the Landsat Ice Speed of Antarctica (LISA; (Scambos et al., 2019)). The LISA displacement values were generated from July 2016 to April 2017 Landsat 8 OLI imagery and has a spatial resolution of 750 m.

3 Results

3.1 Basal crevasse geometry

The floating base of Byrd Glacier is heavily crevassed within the fjord and out on RIS. Both observational and modeling results reveal that Byrd Glacier is susceptible to crevassing of varying sizes and clusters.

3.1.1 Observed crevasse locations and heights

We identify ∼300 basal crevasses from the 2011/12 CReSIS echograms (Figure 3). Crevasse distribution is most dense within the glacier fjord, and decreases as ice flows into the RIS. Crevasses range in height from ∼40 – 335 m and ∼0.08–1.2 km in width. Hyperbole found in echograms collected near the glacier margins were ignored because high shear stresses means those are likely Mode 2 crevasses (Van der Veen, 1998) whose initiation is not exclusively within the grounding zone.

Of the ∼300 hyperbole in Figure 3, we can confidently establish the height of 107 basal crevasses where the apex and both asymptotes are clearly visible. These 100+ crevasses are located within the region of centrally flowing ice where the primary stress is tensile (Whillans et al., 1989) and initial crevasse propagation is due only to extensional stresses in the direction of ice flow (Van der Veen, 1998).

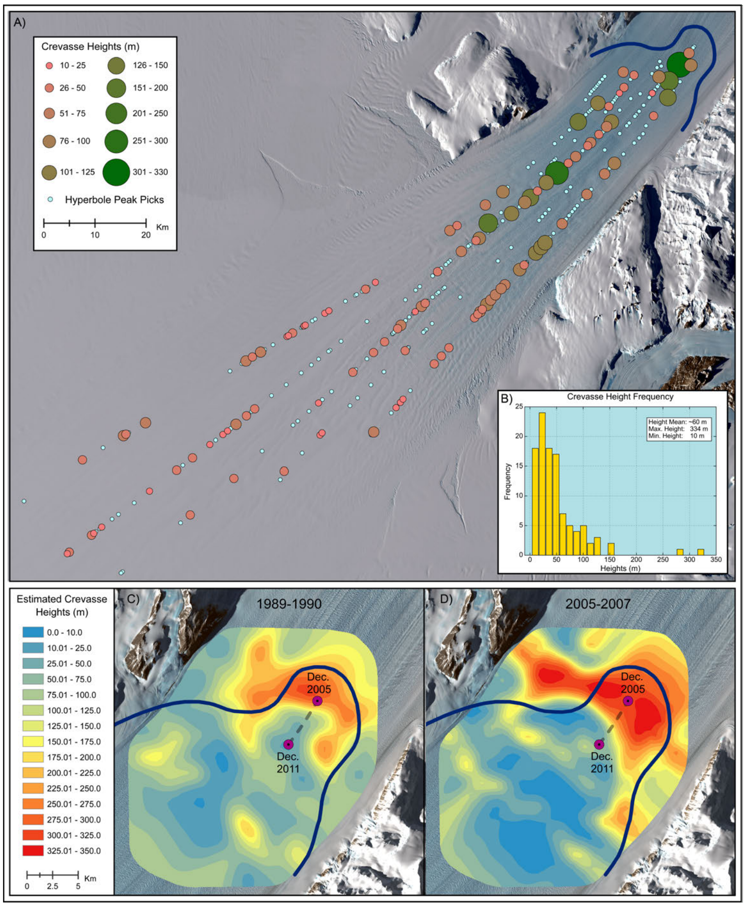

Figure 3. A) Heights for 107 measurable crevasses represented by the green to coral grades in color size gradients. The teal points represent all other basal crevasses. B) A frequency histogram of crevasse heights. C) and D) are the LEFM results for velocities measured in 1989 – 1990 and 2005 – 2007 respectively. The purple points in (C) and (D) represent the approximate location of the ∼335 m tall basal crevasse from December 2005 to December 2011.

3.1.2 Modeled crevasse locations and heights

Due to image availability, it is impossible to pinpoint the exact timing of the acceleration in 2006, but it was likely during the second half of the year (Stearns et al., 2008). LEFM results show that during this time period, crevasse propagation heights within the grounding zone reached ∼285 – 300 m, but only ∼90 – 225 m during a non-flooding period. While both ice flow scenarios demonstrate the largest crevasses forming within the up-flow limit of the grounding zone, the ∼10% increase in speed generates greater tensile rates that result in a ∼75 m taller crevasse height (see Supplemental Information for more detail).

3.1.3 Surface depressions

We identify 28 significant surface depressions over a distance of ∼400 km from Byrd Glacier's grounding line to the RIS terminus (Figure 4). From particle tracking, the oldest surface depression is estimated to have formed ∼600 years ago; the average interval between surface depression formation is 22 years. Most depressions initiated at the furthest up-flow point of the grounding line, but some flow-paths place initiation more south, closer to the Churchill Mountains (Figure 1A).

The 2011/12 radar echograms only overlap with two surface depressions where directly beneath them are large basal crevasses, ∼165 m and ∼290 m tall. We do not observe surface depressions over shorter crevasses. Feature tracking results reveal that the ∼290 m tall crevasse formed ∼1962-1963; however, a surface depression was not observed from satellite imagery until 1990. It took ∼27 – 28 years for a surface depression to form, which aligns well with modeling efforts suggesting that viscous creep is slow at Byrd Glacier (Van der Veen et al., 2014). The basal crevasse that formed in ∼2006 does not currently have a corresponding depression.

4 Discussion

Basal crevasses downflow of Byrd Glacier are not of uniform height. Most crevasses are <50 m tall (Figure 3) and do not form surface depressions. We infer the 28 observed surface depressions overlie large basal crevasses and we hypothesize that these large basal crevasses form during rapid subglacial drainage events (e.g. Stearns et al. (2008)). These events cause glacier acceleration, which increases the tensile stress at the grounding line. In addition, the large amount of water flowing across the grounding line likely enhances melt of any pre-existing basal crevasse. Below, we outline how these two processes can cause anomalously large basal crevasses to form during drainage events.

4.1 Large basal crevasse formation and glacier acceleration

When ice flow accelerates near the grounding line, tensile stress increases. LEFM results illustrate that with increased tensile stress, basal crevasse heights are predicted to be larger. Ice velocity derived from satellite remote sensing show that Byrd Glacier can flow up to ∼10% faster during subglacial drainage events. This acceleration has the potential to increase crevasse height by ∼25%.

To the best of our knowledge, the only other study to report Antarctic ice shelf basal crevasse heights greater than 300 m is Rist et al. (2002). However, unlike the basal crevasses initiating at Byrd Glacier, those observed by Rist et al. (2002) are rifts (Swithinbank & Lucchitta, 1986). Rifts, though technically basal crevasses, are fractures that have propagated through the entire ice thickness (Cuffey & Paterson, 2010, p.451). The observed rifts from Rist et al. (2002) initiated from the Rutford Ice Stream and do not appear at regular intervals along the Ronne Ice Shelf. It is probable that ice flow from Rutford Ice

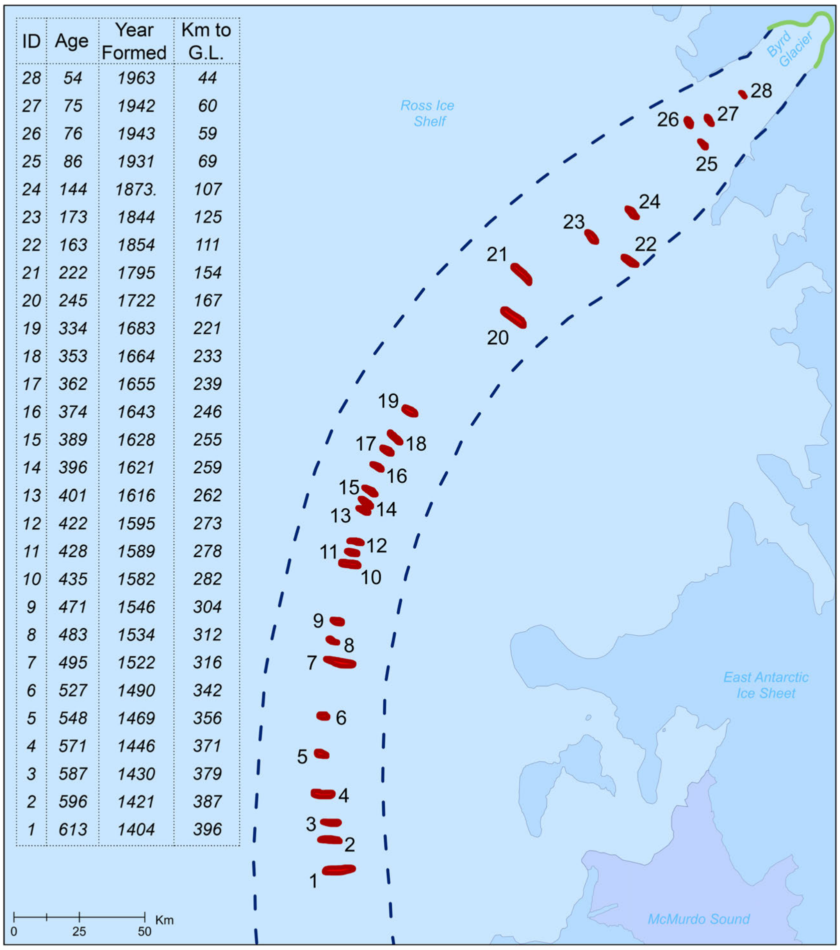

ID	Age	Year Formed	Km to G.L.
28	54	1963	44
27	75	1942	60
26	76	1943	59
25	86	1931	69
24	144	1873.	107
23	173	1844	125
22	163	1854	111
21	222	1795	154
20	245	1722	167
19	334	1683	221
18	353	1664	233
17	362	1655	239
16	374	1643	246
15	389	1628	255
14	396	1621	259
13	401	1616	262
12	422	1595	273
11	428	1589	278
10	435	1582	282
9	471	1546	304
8	483	1534	312
7	495	1522	316
6	527	1490	342
5	548	1469	356
4	571	1446	371
3	587	1430	379
2	596	1421	387
1	613	1404	396

Figure 4. Red polygons show the locations of surface depressions extending from the Byrd Glacier grounding line to the RIS terminus. The age of individual crevasses is shown on the left side of the map; distance from the grounding line (green line) is shown on the right. The dashed blue line is the boundary of Byrd Glacier's ice flow. We do not see any non-rift surface depressions outside of these flowlines.

Stream, like Byrd Glacier, has experienced intermittent acceleration events that have caused episodically large basal crevasses (which became full-fracture rifts).

Rist et al. (2002) hypothesized that short-term variations in ice dynamics cause abnormally large fracturing in Antarctica. While the fractures appear to persist for centuries on Byrd Glacier, they do not seem to influence its stability. On other ice shelves, such as the Larsen C Ice Shelf (Hogg & Gudmundsson, 2017) and the Filchner Ice Shelf (Ferrigno & Gould, 1987), basal crevasses become full-fracture rifts and have led to the calving of considerably large tabular icebergs. To date, no data confirms that the large basal crevasses initiated at Byrd Glacier's grounding line have ever evolved into tabular icebergs via rifts. There is also no evidence demonstrating that Byrd Glacier's abnormally large basal crevasses have any impact on the glacier's or RIS's stability.

4.2 Large basal crevasse formation and subglacial drainage events

LEFM underestimates the height of the ∼335 m tall crevasse by ∼35 – 50 m or ∼12 – 15% of the height derived from radar echograms. A possible explanation for this difference is that LEFM only predicts the initial propagation height and not the evolved height of the crevasse. The emergence of a freshwater plume at the grounding line during a subglacial flood event could have caused additional localized melting (Marsh et al., 2016).

Jenkins (2011) modelled grounding line melt rates for Byrd Glacier when a freshwater plume is the result of a subglacial lake flooding event and when the plume is due to discharge from basal deformational melt. During a flooding event, Jenkins (2011) estimates basal melt of 15.9 m/yr and melt of 5.64 m/yr from non-flood event years.

Lake 2 drained from June 2006 to March 2007 with the greatest amount of drainage occurring within the first five months (Smith et al., 2009; Stearns et al., 2008). Without knowing the month the speedup occurred, we arbitrarily designate November 2006 for the velocity increase and crevasse initiation. Assuming uniform flood influenced melt from December 2006 – March 2007 and only normal melt rates from April 2007 – November 2011, the total melt would be ∼32 m/yr. Combining that amount of deformation with the LEFM results produces a crevasse ∼317 – 332 m tall which is within ∼3 – 18 m of the tallest crevasse's measured height.

In regards to the other abnormally large basal crevasses, it is unknown whether their initiation was also due to Lakes 1 and 2. There are several other subglacial lakes within Byrd Glacier's basin (Smith et al., 2009) and we do not rule out the possibility they could also have caused glacier speedups. Different reservoirs and pathways of flooding basal water could be the reason surface depressions are located on discrete flow-lines.

4.3 Implications

Ice shelves can act as a "plug" for outlet glaciers where their presence maintains stable ice flow (Dupont & Alley, 2005; Depoorter et al., 2013). Through basal melt and iceberg calving, the majority of mass loss in Antarctica occurs at the ice shelf interface (Depoorter et al., 2013; Rignot et al., 2013). There appears to be a direct link between the stability of ice shelves and the mass balance of outlet glaciers draining into the ice shelves; following ice shelf collapses, outlet glaciers undergo sustained accelerations (Scambos et al., 2004). These events can be elicited by weakened buttressing from large calving events triggered by basal crevasses forming rifts (Rott et al., 1996; Hogg & Gudmundsson, 2017). Basal crevasses play an integral role in iceberg formation (Colgan et al., 2016) and provide greater surface area for basal melt processes (Hellmer & Jacobs, 1992).

The subglacial hydrology of Antarctica also affects ice shelf stability from grounding line drainage events. Subglacial channels on ice shelves are known to evolve and grow from the influx of fresh subglacial water (Le Brocq et al., 2013; Marsh et al., 2016; Simkins et al., 2017; Dow et al., 2018) whereby increasing basal surface area for further melt to take place. These melt-induced channels are the initiating factor of forming parallel with ice-flow basal crevasses at the crest of the channels on Pine Island Glacier (Vaughan et al., 2012). This is subsequently another means of crevasse propagation as a consequence of subglacial water influx. The Antarctic basal hydraulic system influences the stability of ice shelves through its impact on glacier dynamics (speed increases leading to crevasse propagation) at the grounding line and melt rates of floating glacier ice. Having a better understanding of the drivers behind basal crevasse production has the potential to aid in better constraining of predictive models about the future of both ice shelves and ice sheets.

5 Conclusion

Byrd Glacier's fjord contains an extensive number of basal crevasses–that propagated from tensile stresses–in a wide range of geometries. We confidently identify the heights and widths for 107 basal crevasses. The spatial pattern of the observed heights appears to be random indicating that Byrd Glacier undergoes intermittent variations in its stress regime.

We also detect a series of surface depressions from the fjord of Byrd Glacier to the terminus of the RIS. The depressions within the fjord are observed to directly overlay abnormally large basal crevasses; we predict that the rest of the depressions in the RIS also overlay abnormally large crevasses. Assuming basal crevasse initiation begins at the grounding line, we use feature tracking to estimate the ages of the depressions to produce a timeline of abnormally large basal crevasse formation expanding over six centuries.

The increased tensile stresses incurred during the 2005-2007 flooding event were large enough to cause an abnormally large basal crevasse. LEFM results, in conjunction with estimated basal melt rates, agree within $\sim 3-18$ m of the observed 2011 height of the $\sim$2006 crevasse. At present, a surface depression has not developed over this basal crevasse, but given the amount of time from crevasse inception to depression formation of the youngest surface depression (Number 28, see Figure 4), we expect a depression to form over the $\sim$335 m tall crevasse within the next $\sim 12-13$ years.

We hypothesize that all abnormally large basal crevasses on Byrd Glacier form as a result of subglacial flooding speedups making basal crevasses proxies for past subglacially induced velocity increases. By tracking the present-day location of surface depressions (e.g. visible markers of abnormally large basal crevasses), to the grounding zone to measure travel times, we create a timeline for 28 past subglacial flooding events.

Acknowledgments

This research was funded by NSF grants ANT0944087 and ANT1255488 awarded to LAS. Gordon S. Hamilton was instrumental in the collection and analysis of the GPS data. The GPS data is available from https://www.usap-dc.org/view/project/p0000319. The radar data was collected and generated by the Center of Remote Sensing of Ice Sheets from the support of the University of Kansas, NSF grant ANT0424589 and NASA Operation IceBridge grant NNX16AH54G available from: ftp://data.cresis.ku.edu/data/rds/2011_Antarctica_TO. The gridded CReSIS products are available via ftp://data.cresis.ku.edu/data/grids/. The surface elevation data were supplied by the Byrd Polar, Climate Research Center, and the Polar Geospatial Center under NSF-OPP awards 1543501, 1810976, 1542736, 1559691, 1043681, 1541332, 0753663, 1548562, 1238993 and NASA award NNX10AN61G. The data is available through: http://data.pgc.umn.edu/elev/dem/setsm/REMA/geocell/v1.0/2m

References

Bentley, C. R. (1987). Antarctic ice streams: a review. *Journal of Geophysical Research: Solid Earth*, *92*(B9), 8843–8858.

Brunt, K. M., Fricker, H. A., Padman, L., Scambos, T. A., & O'Neel, S. (2010). Mapping the grounding zone of the Ross Ice Shelf, Antarctica, using ICESat laser altimetry. *Annals of Glaciology*, *51*(55), 71–79.

Carter, S. P., Fricker, H. A., & Siegfried, M. R. (2017). Antarctic subglacial lakes drain through sediment-floored canals: theory and model testing on real and idealized domains. *The Cryosphere*, *11*(1), 381–405.

Colgan, W., Rajaram, H., Abdalati, W., McCutchan, C., Mottram, R., Moussavi, M. S., & Grigsby, S. (2016). Glacier crevasses: Observations, models, and mass balance implications. *Reviews of Geophysics*, *54*(1), 119—161.

Comiso, J. C., Gersten, R. A., Stock, L. V., Turner, J., Perez, G. J., & Cho, K. (2017). Positive trend in the Antarctic sea ice cover and associated changes in surface temperature. *Journal of Climate*, *30*(6), 2251–2267.

CReSIS. (2014). *Antarctica 2011 Twin Otter Data, Lawrence, Kansas, USA. Digital Media.* Retrieved from `http://data.cresis.ku.edu/`

Cuffey, K. M., & Paterson, W. S. B. (2010). *The physics of glaciers.* Academic Press.

Depoorter, M. A., Bamber, J., Griggs, J., Lenaerts, J. T., Ligtenberg, S. R., van den Broeke, M. R., & Moholdt, G. (2013). Calving fluxes and basal melt rates of Antarctic ice shelves. *Nature*, *502*, 89–92.

Dow, C. F., Lee, W. S., Greenbaum, J. S., Greene, C. A., Blankenship, D. D., Poinar, K., … Zappa, C. J. (2018). Basal channels drive active surface hydrology and transverse ice shelf fracture. *Science Advances*, *4*(6).

Dupont, T. K., & Alley, R. B. (2005). Assessment of the importance of ice-shelf buttressing to ice-sheet flow. *Geophysical Research Letters*, *32*(4).

Elósegui, P., Davis, J. L., Johansson, J. M., & Shapiro, I. I. (1996). Detection of transient motions with the Global Positioning System. *Journal of Geophysical Research: Solid Earth*, *101*(B5), 11249–11261.

Elósegui, P., Davis, J. L., Oberlander, D., Baena, R., & Ekström, G. (2006). Accuracy of high-rate GPS for seismology. *Geophysical Research Letters*, *33*(11).

Fahnestock, M., Scambos, T., Moon, T., Gardner, A., Haran, T., & Klinger, M. (2016). Rapid large-area mapping of ice flow using Landsat 8. *Remote Sensing of Environment*, *185*, 84–94.

Ferrigno, J. G., & Gould, W. G. (1987). Substantial changes in the coastline of Antarctica revealed by satellite imagery. *Polar Record*, *23*(146), 577–583.

Fretwell, P., Pritchard, H. D., Vaughan, D. G., Bamber, J. L., Barrand, N. E., Bell, R., … Zirizzotti, A. (2013). Bedmap2: improved ice bed, surface and thickness datasets for Antarctica. *The Cryosphere*, *7*(1), 375–393.

Fricker, H. A., & Padman, L. (2006). Ice shelf grounding zone structure from ICESat laser altimetry. *Geophysical Research Letters*, *33*(15).

Glennie, C. (2018). Arctic high-resolution elevation models: Accuracy in sloped and vegetated terrain. *Journal of Surveying Engineering*, *144*(1).

Gogineni, S., Yan, J.-B., Paden, J. D., Leuschen, C. J., Li, J., Rodriguez-Morales, F., … Gauch, J. (2014). Bed topography of Jakobshavn Isbræ, Greenland, and Byrd Glacier, Antarctica. *Journal of Glaciology*, *60*(223), 813–833.

Haran, T., Bohlander, J., Scambos, T., Painter, T., & Fahnestock, M. (2014). MODIS Mosaic of Antarctica 2008–2009 (MOA2009) image map, Version 1 (Updated 2019). *Boulder, Colorado USA, National Snow and Ice Data Center*. (Accessed: October 9, 2019) doi: https://doi.org/10.7265/N5KP8037

Hellmer, H. H., & Jacobs, S. S. (1992). Ocean interactions with the base of Amery Ice Shelf, Antarctica. *Journal of Geophysical Research: Oceans*, *97*(12).

Hogg, A. E., & Gudmundsson, G. H. (2017). Impacts of the Larsen-C Ice Shelf calving event. *Nature Climate Change*, *7*(8), 540–542.

Hooke, R. L. (1981). Flow law for polycrystalline ice in glaciers: comparison of theoretical predictions, laboratory data, and field measurements. *Reviews of Geophysics*, *19*(4), 664–672.

Howat, I. M., Porter, C., Smith, B. E., Noh, M.-J., & Morin, P. (2019). The reference elevation model of antarctica. *The Cryosphere*, *13*(2), 665–674.

Hulbe, C., & Fahnestock, M. (2007). Century-scale discharge stagnation and reactivation of the Ross ice streams, West Antarctica. *Journal of Geophysical Research: Earth Surface*, *112*(3).

Humbert, A., Steinhage, D., Helm, V., Hoerz, S., Berendt, J., Leipprand, E., ... Müller, R. (2015). On the link between surface and basal structures of the Jelbart Ice Shelf, Antarctica. *Journal of Glaciology*, *61*(229), 975-–986.

Jenkins, A. (2011). Convection-driven melting near the grounding lines of ice shelves and tidewater glaciers. *Journal of Physical Oceanography*, *41*(12), 2279–2294.

Jenson, S. K., & Domingue, J. O. (1988). Extracting topographic structure from digital elevation data for geographic information system analysis. *Photogrammetric Engineering and Remote Sensing*, *54*(11), 1593–1600.

Jezek, K. C. (1984). A modified theory of bottom crevasses used as a means for measuring the buttressing effect of ice shelves on inland ice sheets. *Journal of Geophysical Research: Solid Earth*, *89*(3).

Jezek, K. C., & Bentley, C. R. (1983). Field studies of bottom crevasses in the Ross Ice Shelf, Antarctica. *Journal of Glaciology*, *29*(101), 118-–126.

Jezek, K. C., Bentley, C. R., & Clough, J. W. (1979). Electromagnetic sounding of bottom crevasses on the Ross Ice Shelf, Antarctica. *Journal of Glaciology*, *24*(90), 321-–330.

Jimenez, S., & Duddu, R. (2018). On the evaluation of the stress intensity factor in calving models using linear elastic fracture mechanics. *Journal of Glaciology*, *64*(247), 759–770.

Konikow, L. F., & Bredehoeft, J. D. (1978). *Computer model of two-dimensional solute transport and dispersion in ground water* (Vol. 2) (No. 7). US Government Printing Office Washington, DC.

Lai, C.-Y., Kingslake, J., Wearing, M. G., Chen, P.-H. C., Gentine, P., Li, H., ... van Wessem, J. M. (2020). Vulnerability of Antarctica's ice shelves to meltwater-driven fracture. *Nature*, *584*(7822), 574–578.

Le Brocq, A. M., Ross, N., Griggs, J. A., Bingham, R. G., Corr, H. F., Ferraccioli, F., & Jenkins, A. (2013). Evidence from ice shelves for channelized meltwater flow beneath the Antarctic Ice Sheet. *Nature Geoscience*, *6*(11), 945-–948.

LeDoux, C. M., Hulbe, C. L., Forbes, M. P., Scambos, T. A., & Alley, K. (2017). Structural provinces of the Ross Ice Shelf, Antarctica. *Annals of Glaciology*, *58*(75pt1), 88-–98.

Lichten, S. M., & Border, J. S. (1987). Strategies for high-precision Global Positioning System orbit determination. *Journal of Geophysical Research: Solid Earth*, *92*(B12), 12751–12762.

Livingstone, S., Clark, C., Woodward, J., & Kingslake, J. (2013). Potential subglacial lake locations and meltwater drainage pathways beneath the Antarctic and Greenland ice sheets. *Cryosphere*, *7*(6), 1721–1740.

Luckman, A., Jansen, D., Kulessa, B., Edward King, P., & Benn, D. (2012). Basal crevasses in Larsen C Ice Shelf and implications for their global abundance. *The Cryosphere*, *6*(1), 113—123.

Marsh, O. J., Fricker, H. A., Siegfried, M. R., Christianson, K., Nicholls, K. W., Corr, H. F., & Catania, G. (2016). High basal melting forming a channel at the grounding line of Ross Ice Shelf, Antarctica. *Geophysical Research Letters*, *43*(1), 250-–255.

McGrath, D., Steffen, K., Scambos, T., Rajaram, H., Casassa, G., & Lagos, J. L. R. (2012). Basal crevasses and associated surface crevassing on the Larsen C ice shelf, Antarctica, and their role in ice-shelf instability. *Annals of Glaciology*,

53(60), 10-–18.
McNabb, R. (2019). *Pybob: A python package of geospatial tools.* Github. Retrieved from `https://github.com/iamdonovan/pybob` (Version 0.25)
Noh, M.-J., & Howat, I. M. (2015). Automated stereo-photogrammetric DEM generation at high latitudes: Surface Extraction with TIN-based Search-space Minimization (SETSM) validation and demonstration over glaciated regions. *GIScience and Remote Sensing*, *52*(2), 198-–217.
Nuth, C., & Kääb, A. (2011). Co-registration and bias corrections of satellite elevation data sets for quantifying glacier thickness change. *The Cryosphere*, *5*(1), 271-–290.
O'Callaghan, J. F., & Mark, D. M. (1984). The extraction of drainage networks from digital elevation data. *Computer Vision, Graphics, and Image Processing*, *28*(3), 323–344.
Pavlis, N. K., Holmes, S. A., Kenyon, S. C., & Factor, J. K. (2012). The development and evaluation of the Earth Gravitational Model 2008 (EGM2008). *Journal of Geophysical Research: Solid Earth*, *117*(B4).
Rignot, E., Jacobs, S., Mouginot, J., & Scheuchl, B. (2013). Ice-shelf melting around Antarctica. *Science*, *341*(6143), 266-–270.
Rist, M., Sammonds, P., Murrell, S., Meredith, P., Doake, C., Oerter, H., & Matsuki, K. (1999). Experimental and theoretical fracture mechanics applied to Antarctic ice fracture and surface crevassing. *Journal of Geophysical Research: Solid Earth*, *104*(B2), 2973–2987.
Rist, M., Sammonds, P., Murrell, S., Meredith, P., Oerter, H., & Doake, C. (1996). Experimental fracture and mechanical properties of Antarctic ice: preliminary results. *Annals of glaciology*, *23*, 284–292.
Rist, M., Sammonds, P., Oerter, H., & Doake, C. (2002). Fracture of Antarctic shelf ice. *Journal of Geophysical Research: Solid Earth*, *107*(1), ECV 2.1–ECV 2.13.
Rott, H., Skvarca, P., & Nagler, T. (1996). Rapid collapse of northern Larsen ice shelf, Antarctica. *Science*, *271*(5250), 788–792.
Sandhäger, H., Rack, W., & Jansen, D. (2005). Model investigations of larsen b ice shelf dynamics prior to the breakup. *FRISP Rep*, *16*, 5–12.
Scambos, T. A., Bohlander, J., Shuman, C., & Skvarca, P. (2004). Glacier acceleration and thinning after ice shelf collapse in the Larsen B embayment, Antarctica. *Geophysical Research Letters*, *31*(18).
Scambos, T. A., Dutkiewicz, M. J., Wilson, J. C., & Bindschadler, R. A. (1992). Application of image cross-correlation to the measurement of glacier velocity using satellite image data. *Remote sensing of environment*, *42*(3), 177–186.
Scambos, T. A., Fahnestock, M., Moon, T., Gardner, A., & Klinger, M. (2019). *Ice Speed of Antarctica (LISA), Version 1. [2016-2017].* Retrieved from `https://doi.org/10.7265/nxpc-e997.`
Shabtaie, S., & Bentley, C. R. (1982). Tabular icebergs: implications from geophysical studies of ice shelves. *Journal of Glaciology*, *28*(100), 413—430.
Shreve, R. L. (1972). Movement of water in glaciers. *Journal of Glaciology*, *11*(62), 205–214.
Simkins, L. M., Anderson, J. B., Greenwood, S. L., Gonnermann, H. M., Prothro, L. O., Halberstadt, A. R. W., . . . DeConto, R. M. (2017). Anatomy of a meltwater drainage system beneath the ancestral East Antarctic ice sheet. *Nature Geoscience*, *10*(9), 691–697.
Smith, B. E., Fricker, H. A., Joughin, I. R., & Tulaczyk, S. (2009). An inventory of active subglacial lakes in Antarctica detected by ICESat (2003–2008). *Journal of Glaciology*, *55*(192), 573–595.
Stearns, L. A., Smith, B. E., & Hamilton, G. S. (2008). Increased flow speed on a large East Antarctic outlet glacier caused by subglacial floods. *Nature Geoscience*, *1*(12), 827–831.

Swithinbank, C., & Lucchitta, B. K. (1986). Multispectral digital image mapping of Antarctic ice features. *Annals of glaciology*, *8*, 159–163.

Tinto, K. J., Padman, L., Siddoway, C. S., Springer, S. R., Fricker, H. A., Das, I., ... Bell, R. E. (2019). Ross Ice Shelf response to climate driven by the tectonic imprint on seafloor bathymetry. *Nature Geoscience*, *12*(6), 441–449.

Van der Veen, C. J. (1998). Fracture mechanics approach to penetration of bottom crevasses on glaciers. *Cold Regions Science and Technology*, *27*(3), 213—223.

Van der Veen, C. J. (2013). *Fundamentals of glacier dynamics*. CRC press.

Van der Veen, C. J., Stearns, L. A., Johnson, J. T., & Csatho, B. M. (2014). Flow dynamics of Byrd Glacier, East Antarctica. *Journal of Glaciology*, *60*(224), 1053–1064.

Van der Veen, C. J., & Whillans, I. M. (1989). Force budget: I. Theory and numerical methods. *Journal of Glaciology*, *35*(119), 53–60.

Vaughan, D. G. (1994). Investigating tidal flexure on an ice shelf using kinematic GPS. *Annals of Glaciology*, *20*, 372-–376.

Vaughan, D. G., Corr, H. F., Bindschadler, R. A., Dutrieux, P., Gudmundsson, G. H., Jenkins, A., ... Wingham, D. J. (2012). Subglacial melt channels and fracture in the floating part of Pine Island Glacier, Antarctica. *Journal of Geophysical Research: Earth Surface*, *117*(F3).

Whillans, I., Chen, Y., Van der Veen, C. J., & Hughes, T. (1989). Force budget: III. Application to three-dimensional flow of Byrd Glacier, Antarctica. *Journal of Glaciology*, *35*(119), 68-–80.

Geophysical Research Letters

Supporting Information for

Basal crevasse formation on Byrd Glacier, East Antarctica as proxy for past subglacial flooding events

Sarah F. Child [1,2], Leigh A. Stearns [1,3], C. J. van der Veen [4], Pedro Elosegui [5,6]

1. Department of Geology, University of Kansas, Lawrence, KS 66045, USA

2. Cooperative Institute for Research in Environmental Sciences, University of Colorado, Boulder, CO580309, USA

3. Center for Remote Sensing of Ice Sheets, University of Kansas, Lawrence, KS 66045, USA

4. Department of Geography & Atmospheric Sciences, University of Kansas, Lawrence, KS 66045, USA

5. Massachusetts Institute of Technology, Haystack Observatory, Westford, MA, 01886 USA

6. Institute of Marine Sciences, ICM-CSIC, Barcelona, Spain, 08003

Contents of this file

Introduction

The following text is additional information about the models and data used in the main manuscript. We expand more on the GPS data, how the hydrostatic equilibrium boundary was determined, how ice thickness was estimated from surface elevation and bed topography data, the effect varying strain rates has on LEFM results, the route of subglacial water within the Byrd Glacier catchment, and tables of the data used in this research.

Text S1. GPS data

We collected geodetic-quality GPS data at a total of 26 locations on Byrd Glacier and three additional sites on surrounding bedrock (Figure S1) over three austral summer campaigns between November 2010 and January 2013. All the sites were equipped with Trimble (NetR9, 5700, or R7) receivers and Trimble Zephyr (55971.00 or 41249.00) antennae—brand and make names are mentioned for identification purposes only. Most of the analysis presented here is based on dual-frequency carrier-beat phase observations collected at nine of the GPS sites straddling the glacier's grounding line over five days in December 2011, with a sampling rate of 30 s.

We used the GIPSY software package (Lichten and Boarder 1987) and high-precision kinematic data processing methods (e.g., Elosegui et al., (1996, 2006)) to estimate glacier GPS sites' time-varying positions once every 300 s. Precise satellite orbits from the International GNSS Service (IGS) were employed with no further orbit improvement. For each 300 s epoch, we estimated receiver clock errors, modeled as white noise stochastic process, as well as atmospheric zenith delays and the motion of the moving antenna, with the last two set of parameters modeled as random walk stochastic processes. Only observations above a minimum elevation angle of 7º were used.

The GPS analysis provides, among other parameters, stochastic-filter-smoothed time-dependent adjustments to the *a priori* values of the three-dimensional position parameters for each site. These adjustments (less a mean) are shown for nine of the GPS sites in Figure 1C for the vertical component of site position in a topocentric frame, e.g., a frame defined by the *a priori* position of the site in which the adjustments are expressed as relative position with cartesian components east, north, and vertical (positive up). The sites down-glacier from the grounding line exhibit dominant vertical position diurnal variations that can reach up to ~1 m peak-to-peak, indicative of tidal influences. The estimated formal uncertainties of vertical positions for the nine GPS sites range was 2—5 cm over the 3-month austral summer deployment of 2011/2012. The weighted root-mean-square (rms) scatter of vertical position estimates are derived from the weighted mean of the three rock sites over the entire deployment time (~2.25 years). Although the rock sites are obviously static, their GPS data were also processed using the same high-precision kinematic technique applied to the glacier sites hence providing an estimate of positioning precision for the latter.

Text S2. Hydrostatic Equilibrium

The hydrostatic equilibrium (H_e) was estimated using the buoyancy calculation,

$$H_e = h - \left(H * \left[\frac{\rho_w - \rho_i}{\rho_w}\right]\right) \tag{1}$$

where h is the present-day surface elevation, H is the ice thickness, and ρ_i, ρ_w are the ice and water density, respectively. The down-flow extent of the grounding zone is located where this value is approximately zero (when h is projected in orthometric heights) and ice begins to float. The data used for these parameters (h and H) are described below.

Text S3. Ice thickness data

Ice thickness was calculated by subtracting the picked CReSIS echogram bed topography from the surface elevation data, described below. Both data sets were converted from their WGS84 ellipsoidal heights to orthometric ones using the EGM2008 model (Pavlis et al., 2012).

Bed elevation

The bed elevation is point data from the manually picked CReSIS echograms CReSIS, which is available from their L3 product of Byrd Glacier. The bed elevation is referenced vertically to the WGS84 ellipsoid and horizontally in WGS84 polar stereographic. Sources of error in the point data come from the geolocation of the airborne platform uncertainties, range measurement uncertainties, and bed interpretation error of echogram picking (Gogineni et al., 2014). Crossover analysis of overlapping flight paths resulted in a mean ice thickness error of ~30.64 m with a standard deviation of ~39.88 m (CReSIS, 2014, Gogineni et al., 2014).

Surface elevation

Our surface DEM is from 25 2 m resolution DEM strips generated from WorldView 1, 2, 3 imagery using the Surface Extraction with TIN-based Search-space Minimization (SETSM) algorithm by Noh and Howat (2015). For imagery collected at low degrees of off-nadir over regions with a high density of ground control, the accuracy of these products is assessed at ~1 m (Howat et al. 2019). Over Byrd Glacier, the off-nadir angle varied from 6º—29º and ground control is sparse, so the error is likely higher than the Howat et al. (2019) estimate and we assume a value of 5 m like that of Glennie (2018). We found in the 2 m DEMs that blunders existed from cloud cover, shadows, and the backside of terrain where image acquisition was impossible due to off-nadir (e.g. >20°) collection. These blunders were manually clipped from the DEMs and then each strip was coregistered to its closest neighbor upstream using the Nuth and Kääb (2011) method in McNabb (2019)'s python module PyBob. This method of co-registering was a means of maintaining a cohesive data registration before the strips were mosaicked to a grid of 5 m and referenced to the WGS84 ellipsoid.

Text S4. Velocity Data

Byrd Glacier Velocities

The velocity data for a non-flooding period were calculated from band 4 of Landsat 4 TM imagery collected in 1989 and 1990 (Stearns, 2007). The velocities from a flooding period are from Stearns et. al, (2008) and estimated from ASTER and ALOS AVNIR-2 data (collected from 2005-2007). Both sets were and processed in the Image Cross-Correlation (IMCORR) software which uses a feature tracking algorithm to determine the magnitude and direction of displacement (Scambos et. al., 1992) (see Figure S4).

Ross Ice Shelf Velocities

The feature tracking estimations were conducted using a mosaic of glacier surface velocities generated from Landsat 8 OLI imagery called the Landsat Ice Speed of Antarctica (LISA) (Scambos et al., 2019). Velocities were estimated using a feature tracking program called PyBob (Fahnestock et al., 2016). LISA mosaics have a spatial resolution of 750 m and the velocities used in the mosaic for this study were from imagery acquired over July 1, 2016 to April 30, 2017.

Text S5. The effect of increased strain rates on LEFM results

No radar data was collected during the flood period of 2005-2007, so we were unable to measure any newly formed basal crevasses during this time period. We instead used LEFM to model estimated basal crevasse heights based on surface velocities from a time of increased speeds and a time of normal ice flow. LEFM is an appropriate model to use in this circumstance because the crevasse height does not propagate to more than 60% of the glacier thickness (Jiménez and Duddu, 2018; Lai et al., 2020). Because it is assumed that crevasses propagate quickly from large tensile rates (Cuffey and Patterson, 2010, pp 450-451), we treat ice as an elastic solid (Luckman et. al., 2012). LEFM calculates a stress intensity factor (K_I). The theory is that as long as this stress intensity factor is greater than a fracture criterion, or ice toughness, then a crack will propagate assuming the presence of a small (.5—2.0 m) starter crack (Rist et al., 1996; van der Veen, 1998).

$$K_I = \int_0^h \frac{2\sigma_n(z)}{\sqrt{\pi h}}\, G(\gamma,\lambda)\, dz \tag{2}$$

$G(\gamma,\lambda)$ is a function of $\lambda = {}^{h}/_{H}$ and $\gamma = {}^{z}/_{h}$ established by fitting a polynomial curve to modelled stress intensity factor values (van der Veen, 1998). h is the crevasse height, H the ice thickness, and z the depth within the glacier where $z = 0$ at the glacier base and $z = H$ at the glacier surface:

$$G(\gamma,\lambda) = \frac{3.52(1-\gamma)}{(1-\lambda)^{3/2}} - \frac{4.35-5.28\gamma}{(1-\lambda)^{\frac{1}{2}}} + \left[\frac{1.30-0.03\frac{3}{2}}{(1-\gamma)^{\frac{1}{2}}} + .83 - 1.76\gamma\right] \times [1-(1-\gamma)\lambda] \tag{3}$$

$\sigma_n(z)$ is the combined stresses (tensile, lithostatic, and water pressure) acting at the fracture's tip to either propagate or close the crevasse:

$$\sigma_n(z) = -\rho_i g(H-z) + \frac{\rho_i-\rho_s}{C} g\left[1-e^{-C(H-z)}\right] + \rho_w g\left(H_p - z\right) + R_{xx}(z) \tag{4}$$

The first two terms in equation 4 make up the lithostatic stress; the second term is an empirical relation for ice density (van der Veen, 1998); ρ_s is the density of snow, 350 kg m^{-3}, g is the gravitational potential is 9.8 m/s^2 and C, a constant, is 0.02 m^{-1} after van der Veen (2013, p. 223). The third term is the basal water pressure where H_p is the piezometric head. The last term in equation 4 is the tensile stress. There are no direct measurements of tensile stress, so we modeled it from the strain rates during flooding event velocities and normal flow velocities. The strain rates are related to the tensile stress using van der Veen and Whillans (1989)'s glacier ice flow law through the rate factor. We treated the strain rates are treated as non-varying with depth because of the assumption that basal crevasses form at the grounding line where ice is floating. Increased speeds from the 2006 flooding event also increased the strain rates which is the largest influence on resulting basal crevasse heights (van der Veen, 1998) (see Figure S5).

We used Hooke (1981)'s rate factor as varying with depth which we calculated with Sandhäger et. al., (2005)'s depth-varying temperature profile with estimated surface and bottom temperatures of -20°C (van der Veen et al. 2014) and -1.9°C (Tinto et al., 2019) respectively. We estimate basal crevasse heights assuming a critical toughness value of .155 $MPa\, m^{1/2}$ because, to the best of our knowledge, it is the only measured ice toughness value from an Antarctic ice shelf (Rist et al., 1999). This toughness value was determined from an ice core sample from the Ronne Ice Shelf (Rist et al. 1999), but considering Byrd Glacier and the grounding line of the Ronne Ice Shelf have similar surface temperatures (Comiso et al, 2017), and ice thicknesses (Fretwell et al. 2013), we assume it is appropriate to use the same criterion.

LEFM calculations were applied to gridded point data over a ~20x30 km region within the grounding zone. The differing parameters at each point were strain rates and ice thickness values. The resulting basal crevasse heights were then interpolated in ArcMap using ordinary kriging to a new grid of 500 m spatial resolution (the same as the CReSIS grid).

Text S6. Subglacial water pathways

It is beyond the scope of this study to identify whether the type of subglacial water flow is channelized or film, and we do not include an analysis of a coupled hydrology and glacier dynamic model. We are interested to know the approximate locations of subglacial flood pathways to show that water from lakes will indeed drain at the Byrd Glacier grounding line and not at another outlet glacier. The grounding line exit location is also likely where freshwater plumes form and cause localized melt features in Antarctic ice shelves (Jenkins, 2011; Carter and Fricker, 2012; Le Brocq et. al., 2013; Marsh et. al., 2015).

Basal water pathways are estimated using a similar method to Livingstone et. al., (2013) which relies on the ArcGIS 10.6 toolset to derive hydrological pathways (based on O'Callaghan and Mark (1984)'s method). Water routes follow the direction of the largest hydraulic gradient which is estimated from Shreve (1972):

$$\Phi_h = \rho_i g h + (\rho_w - \rho_i) g (h - H) \tag{5}$$

The hydraulic gradient is then used to solve for the hydraulic head (Cuffey and Patterson, 2010 p.194):

$$Q = \frac{\Phi_h}{\rho_w g} \tag{6}$$

The hydraulic head is plugged in an 8-directional flow model by Jenson and Domingue (1988) to estimate the direction of subglacial water flow. The final step is estimating the flow accumulation which produces probable basal water pathways (Figure S6).

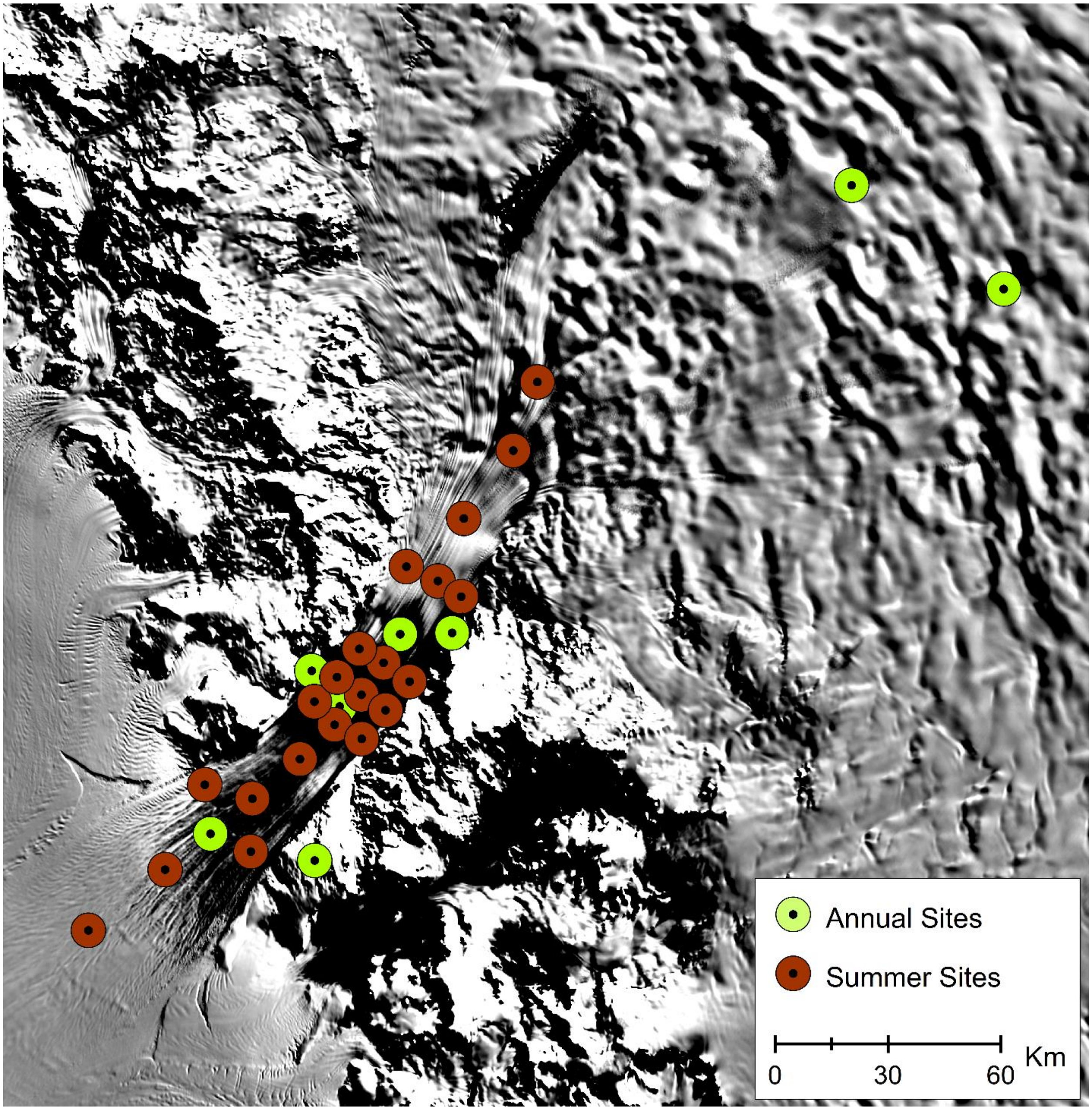

Figure S1. A map of the 29 GPS receivers deployed on Byrd Glacier from the two subglacial lakes to the floating portion on RIS over the duration of 2010-2013. The background image is from Haran et al. (2014) and available from NSIDC.

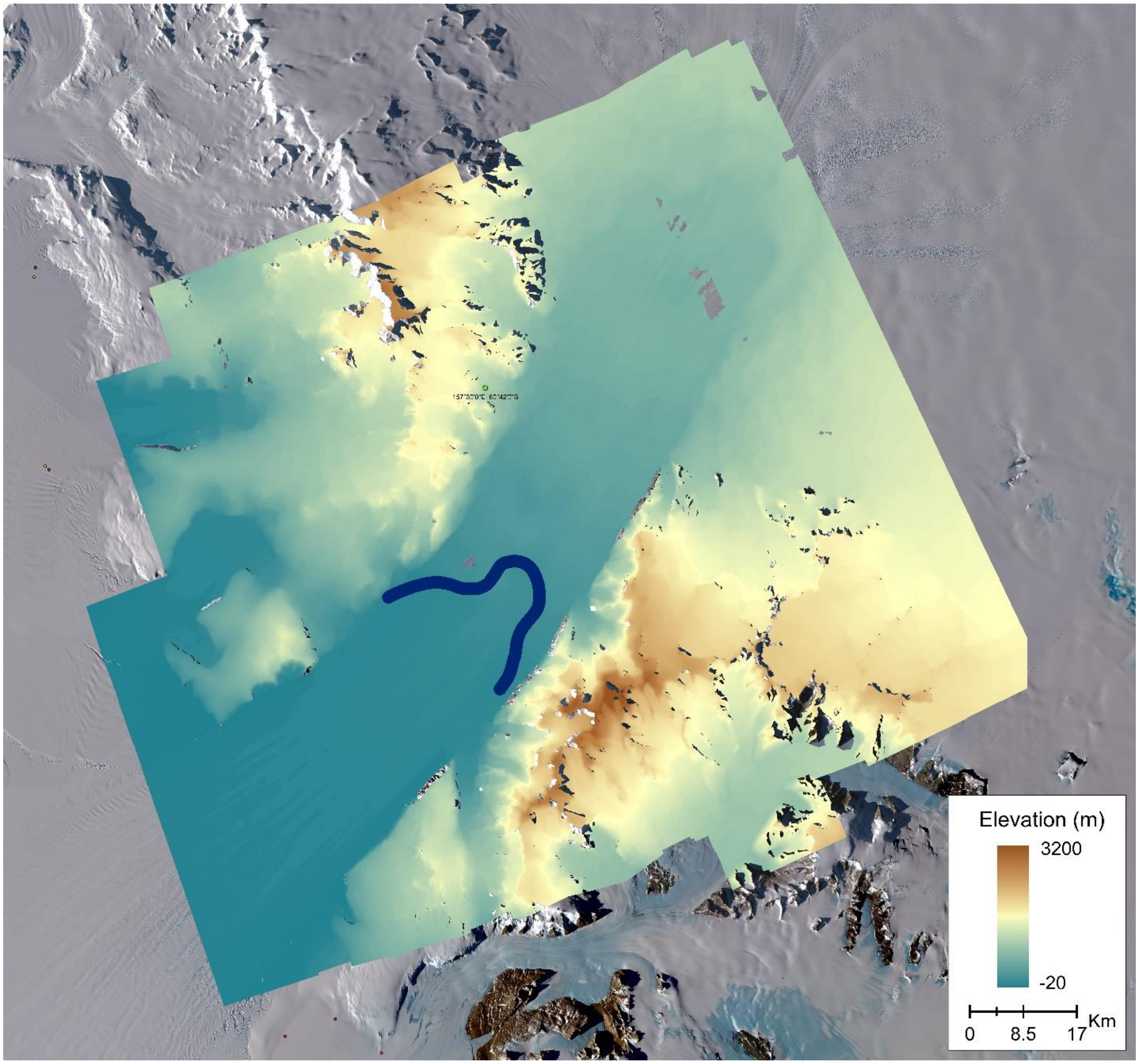

Figure S2. The final REMA DEM strip mosaic. The background is a band composite of Landsat 8 OCI's LC08_L1GT_047118_20190217_20190222_01_T2 and LC08_L1GT_047119_20190217_20190222_01_T2.

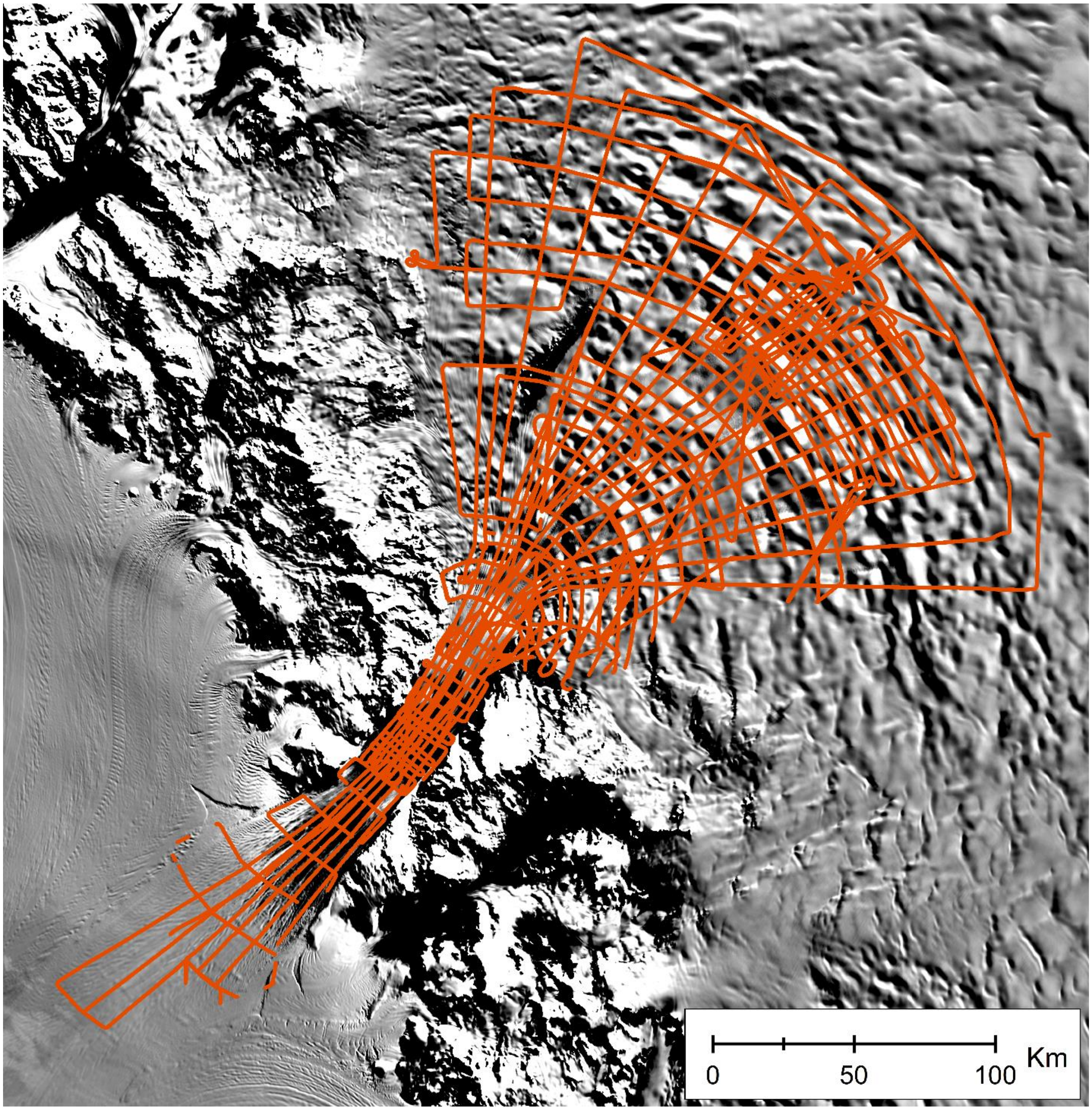

Figure S3. CReSIS flight paths in orange from the 2011-12 data collection over Byrd Glacier. All of the data used in this study are concentrated to the lower half of the glacier. These are the data used to generate the bedrock grid. The background image is from Haran et al. (2014) and available from NSIDC.

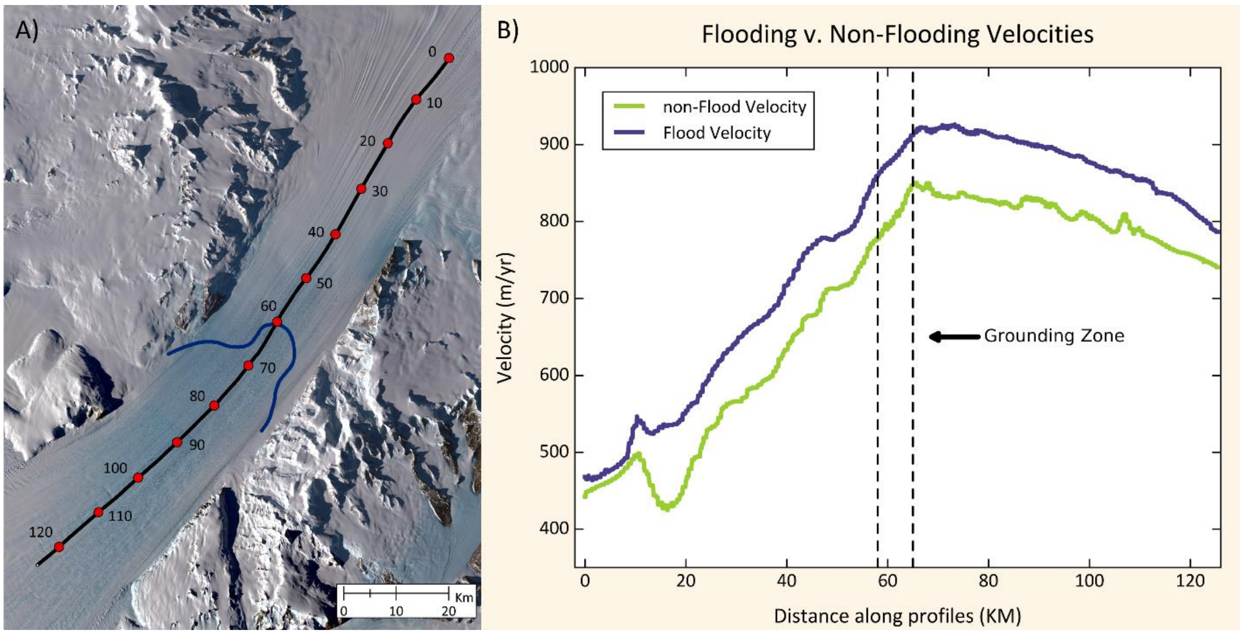

Figure S4. Plot of surface velocities (B) from a flooding period and a non-flooding period along a flow-path (A).

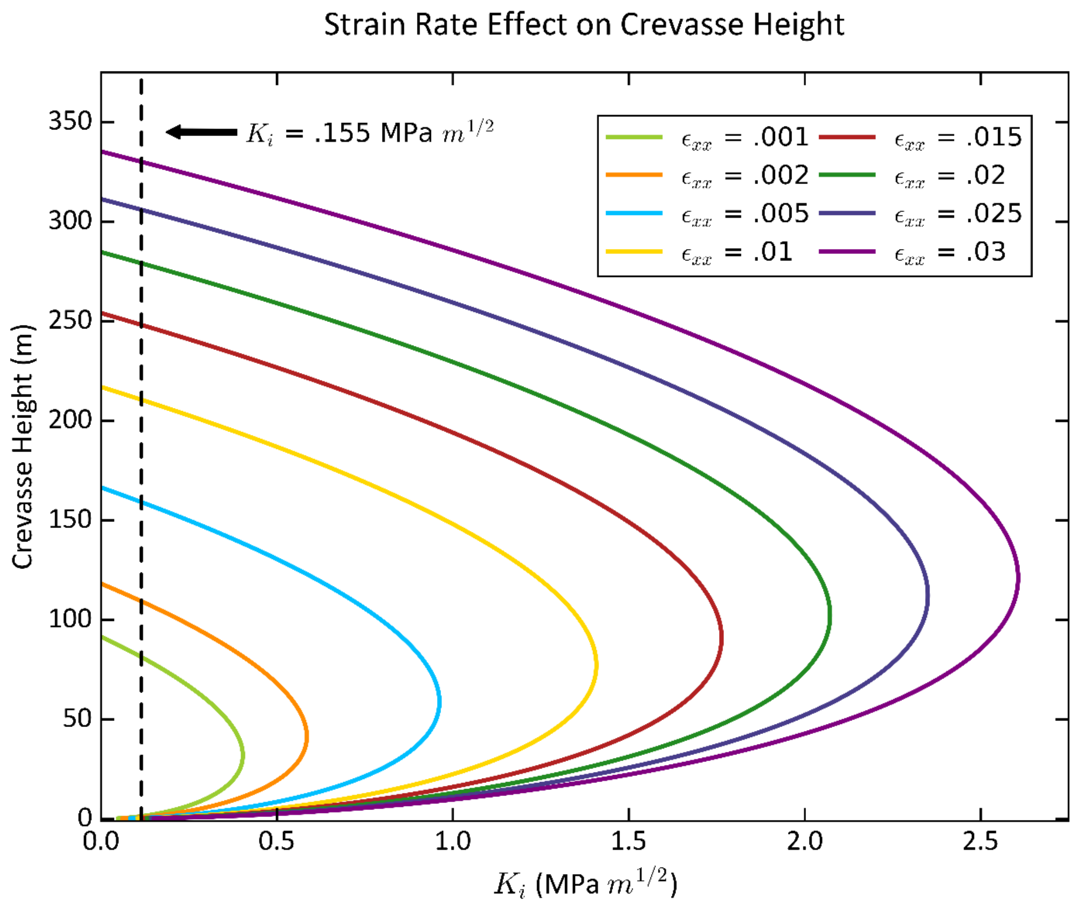

Figure S5. Crevasse height results with varying strain rates. Strain rate (ε_{xx}) values are in units of meters per year. In this example, the average ice thickness value within Byrd Glacier's grounding zone of 1,800 m was used. We estimated crevasse heights with the same stress intensity value of .155 $MPa\ m^{1/2}$(black dashed line), measured by Rist et al., (1999), from the Ronne Ice Shelf.

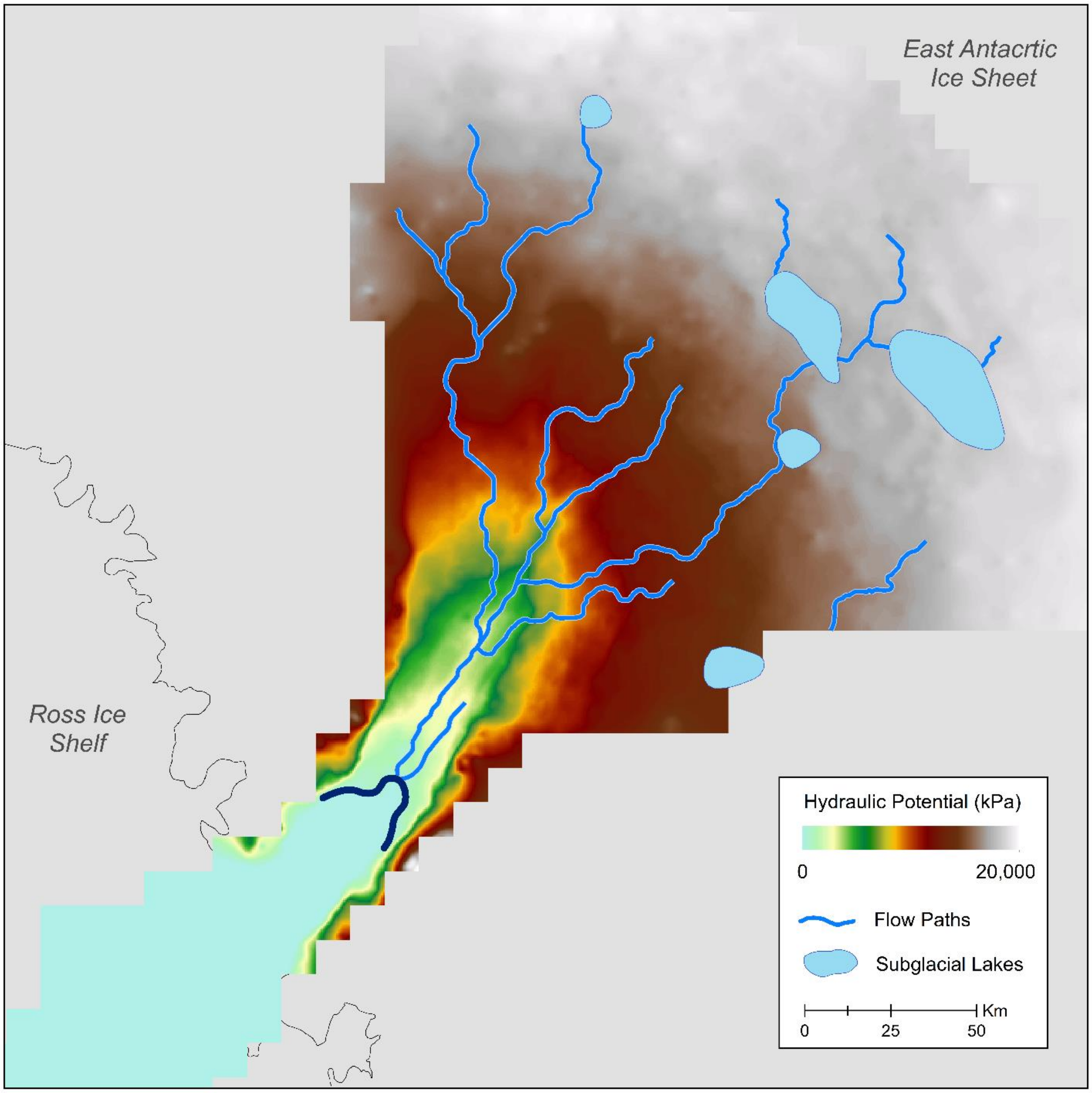

Figure S6. Map of hydraulic potential over Byrd Glacier's catchment basin to the grounding line. The subglacial lake locations are from Smith et al. (2009) and the light blue lines represent the path of substantial water flow.

REMA 2 m Strips
WV01_20170117_102001005B5DCE00_102001005D03ED00_seg1_2m_dem.tif
WV01_20161022_10200100572C2600_102001005728F300_seg1_2m_dem.tif
WV02_20170114_1030010063357E00_103001006328C800_seg1_2m_dem.tif
WV02_20170112_1030010063C79200_1030010064666E00_seg1_2m_dem.tif
WV02_20161104_103001005E85A100_1030010061CB4700_seg1_2m_dem.tif
WV03_20170106_1040010026CC6900_10400100263B2100_seg1_2m_dem.tif
WV02_20161106_103001005DB42D00_103001005D998800_seg1_2m_dem.tif
WV02_20161104_103001005FB39200_103001005F580E00_seg1_2m_dem.tif
WV02_20161103_103001005D2CB600_103001005F7E5300_seg3_2m_dem.tif
WV01_20170112_102001005E897C00_1020010059681600_seg1_2m_dem.tif
WV01_20170220_102001005BB1E700_102001005B62C700_seg1_2m_dem.tif
WV03_20170220_1040010029C88300_1040010029A3F500_seg1_2m_dem.tif
WV01_20170106_10200100596C6200_1020010059CA5F00_seg1_2m_dem.tif
WV01_20161105_10200100596C1200_102001005681D700_seg1_2m_dem.tif
WV01_20170112_102001005D748700_102001005DAFDE00_seg1_2m_dem.tif
WV02_20160204_1030010050525F00_1030010051D1C200_seg1_2m_dem.tif
WV01_20161107_102001005A3DD700_1020010056A10100_seg1_2m_dem.tif
WV01_20160204_1020010049146A00_1020010047BD2A00_seg1_2m_dem.tif
WV01_20170121_102001005AC91A00_102001005A582200_seg1_2m_dem.tif
WV03_20170123_104001002827D100_104001002891ED00_seg1_2m_dem.tif
WV01_20160201_102001004ACC8100_10200100468C3C00_seg1_2m_dem.tif
WV01_20160120_10200100487B0B00_102001004C1AF200_seg1_2m_dem.tif
WV01_20170122_102001005A724300_10200100594FD400_seg1_2m_dem.tif
WV01_20170130_102001005C044C00_102001005C1ACD00_seg1_2m_dem.tif
WV03_20161103_10400100239D2200_10400100231A1300_seg1_2m_dem.tif
CReSIS Data
Data_20111201_05_005
Data_20111205_08_003
Data_20111214_02_010
Data_20111214_02_012
Data_20111214_06_002
Data_20111214_06_003
Data_20111214_06_004
Data_20111216_03_002
Data_20111216_04_001
Data_20111216_04_003
Data_20111218_01_002
Data_20111218_01_003
Data_20111218_03_003
Data_20111218_03_005
Data_20111218_03_006

Data_20111218_03_007
Data_20111218_04_001
Data_20111218_04_009
Data_20111218_05_001
Data_20111218_05_003
CReSIS Point Data
Byrd_2011_Composite
Landsat 8 OLI Scenes
LC08_L1GT_046117_20161202_20170317_01_T2_B8.TIF
LC08_L1GT_047116_20161209_20170317_01_T2_B8.TIF
LC08_L1GT_047117_20170110_20170311_01_T2_B8.TIF
LC08_L1GT_048116_20170202_20170215_01_T2_B8.TIF
LC08_L1GT_048117_20170202_20170215_01_T2_B8.TIF
LC08_L1GT_048118_20170202_20170215_01_T2_B8.TIF
LC08_L1GT_049117_20170124_20170311_01_T2_B8.TIF
LC08_L1GT_050115_20170216_20170228_01_T2_B8.TIF
LC08_L1GT_050116_20170216_20170228_01_T2_B8.TIF
LC08_L1GT_050117_20161112_20170318_01_T2_B8.TIF
LC08_L1GT_050118_20161214_20170316_01_T2_B8.TIF
LC08_L1GT_051115_20170223_20170301_01_T2_B8.TIF
LC08_L1GT_051116_20170223_20170301_01_T2_B8.TIF
LC08_L1GT_051117_20170223_20170301_01_T2_B8.TIF
Velocity Data
lisa750_2016183_2017120_0000_0400_v1

Table S1. A list of all the data sets, not including the GPS data from the 2010-2013 field seasons, used in the analysis of this research. Information to access these data is in the acknowledgements section of the main text.

SI References (also listed in main text Reference section)

Carter, S. P., Fricker, H. A., and Siegfried, M. R. (2017). Antarctic subglacial lakes drain through sediment-floored canals: theory and model testing on real and idealized domains. *The Cryosphere*, *11*(1), 381-405.

Comiso, J.C., Gersten, R.A., Stock, L.V., Turner, J., Perez, G.J. and Cho, K. (2017). Positive trend in the Antarctic sea ice cover and associated changes in surface temperature. *Journal of Climate*, *30*(6), 2251-2267.

CReSIS. (2014). Antarctica 2011 Twin Otter Data, Lawrence, Kansas, USA. Digital Media. Retrieved from http://data.cresis.ku.edu/.

Cuffey, K. M., and Paterson, W. S. B. (2010). *The physics of glaciers*. Academic Press. pp. 194, 450-451.

Elosegui, P., J. L. Davis, J. M. Johansson, and I. I. Shapiro. (1996). Detection of Transient Motions with the Global Positioning System. *Journal of Geophysical Research: Solid Earth, 101*(B5), 11249–11261.

Elosegui, P., Davis, J. L., Oberlander, D., Baena, R., and Ekström, G. (2006). Accuracy of High-Rate GPS for Seismology. *Geophysical Research Letters, 33*(11).

Fahnestock, M., T. Scambos, T. Moon, A. Gardner, T. Haran, and M. Klinger. (2016). Rapid large-area mapping of ice flow using Landsat 8, *Remote Sensing of Environment, 185*. 84-94. https://doi.org/10.1016/j.rse.2015.11.023

Fretwell, P., Pritchard, H.D., Vaughan, D.G., Bamber, J.L., Barrand, N.E., Bell, R., Bianchi, C., Bingham, R.G., Blankenship, D.D., Casassa, G. and Catania, G. (2013). Bedmap2: improved ice bed, surface and thickness datasets for Antarctica. *The Cryosphere*, *7*(1), 375-393.

Glennie, C. (2018). Arctic high-resolution elevation models: Accuracy insloped and vegetated terrain. *Journal of Surveying Engineering 144*(1).

Gogineni, S., Yan, J.-B., Paden, J. D., Leuschen, C. J., Li, J., Rodriguez-Morales, F., Braaten, D.A., Purdon, K., Wang, Z., Liu, W. and Gauch, J. (2014). Bed topography of Jakobshavn Isbræ, Greenland, and Byrd Glacier, Antarctica. *Journal of Glaciology, 60*(223), 813-833.

Haran, T., Bohlander, J., Scambos, T. Painter, T., and Fahnestock, M. (2014). *MODIS Mosaic of Antarctica 2008-2009 (MOA2009) Image Map, Version 1 (updated 2019)*. Boulder, Colorado USA. NASA National Snow and Ice Data Center Distributed Active Archive Center. [October 9, 2019].

Hooke, R. LeB. (1981). Flow law for polycrystalline ice in glaciers: comparison of theoretical predictions, laboratory data, and field measurements. *Reviews of Geophysics*, *19*(4), 664-672.

Howat, I.M., Porter, C., Smith, B.E., Noh, M.J., and Morin, P. (2019). The reference elevation model of Antarctica. *The Cryosphere*, *13*(2), 665-674.

Jenkins, A. (2011). Convection-driven melting near the grounding lines of ice shelves and tidewater glaciers. *Journal of Physical Oceanography*, *41*(12), 2279-2294.

Jenson, S. K. and Domingue, J. O. (1988). Extracting topographic structure from digital elevation data for geographic information system analysis. *Photogrammetric engineering and remote sensing*, *54*(11), 1593-1600.

Jimenez, S. and Duddu, R. (2018). On the evaluation of the stress intensity factor in calving models using linear elastic fracture mechanics. *Journal of Glaciology*, *64*(247), 759-770.

Lai, Ching-Yao, Kingslake, J., Wearing, M. G., Chen, P-H. C., Gentine, P., Li, H., Spergel, J. J., and van Wessem, J. M. (2020). Vulnerability of Antarctica's Ice Shelves to Meltwater-Driven Fracture. *Nature, 584*(7822), 574–578.

Le Brocq, A. M., Ross, N., Griggs, J. A., Bingham, R. G., Corr, H. F., Ferraccioli, F., and Jenkins, A. (2013). Evidence from ice shelves for channelized meltwater flow beneath the Antarctic Ice Sheet. *Nature Geoscience*, *6* (11), 945-948.

Lichten, S. M., and Border, J. S. (1987). Strategies for High-Precision Global Positioning System Orbit Determination. *Journal of Geophysical Research: Solid Earth 92*(B12), 12751–12762.

Livingstone, S., Clark, C., Woodward, J. and Kingslake, J. (2013). Potential subglacial lake locations and meltwater drainage pathways beneath the Antarctic and Greenland ice sheets. *Cryosphere*, *7*(6), 1721-1740.

Luckman, A., Jansen, D., Kulessa, B., Edward King, P., and Benn, D. (2012). Basal crevasses in Larsen C Ice Shelf and implications for their global abundance. *The Cryosphere*, *6*(1), 113-123.

Marsh, O. J., Fricker, H. A., Siegfried, M. R., Christianson, K., Nicholls, K. W., Corr, H. F., and Catania, G. (2016). High basal melting forming a channel at the grounding line of Ross Ice Shelf, Antarctica. *Geophysical Research Letters*, *43*(1), 250-255.

McNabb, R. (2019). PyBob Software, *Download available*: https://github.com/iamdonovan/pybob

Noh, M.-J., and Howat, I. M. (2015). Automated stereo-photogrammetric DEM generation at high latitudes: Surface extraction with tin-based search-space minimization (SETSM) validation and demonstration over glaciated regions. *GIScience Remote Sensing*, *52*(2), 198-217.

Nuth, C., and Kääb, A. (2011). Co-registration and bias corrections of satellite elevation data sets for quantifying glacier thickness change. *The Cryosphere*, *5*(1), 271-290.

O'Callaghan, J.F. and Mark, D.M. (1984). The extraction of drainage networks from digital elevation data. *Computer Vision, Graphics, and Image Processing*, *28*(3), 323-344.

Pavlis, N. K., Holmes, S. A., Kenyon, S. C., and Factor, J. K. (2012). The development and evaluation of the Earth Gravitational Model 2008 (EGM2008). *Journal of geophysical research: Solid Earth*, *117*(B4).

Rist, M., Sammonds, P., Murrell, S., Meredith, P., Doake, C., Oerter, H., and Matsuki, K. (1999). Experimental and theoretical fracture mechanics applied to Antarctic ice fracture and surface crevassing. *Journal of Geophysical Research: Solid Earth*, *104*(B2), 2973–2987.

Sandhäger, H., Rack, W. and Jansen, D. (2005). Model investigations of Larsen B Ice Shelf dynamics prior to the breakup. *FRISP Rep*, *16*, 5-12.

Scambos, T.A., Dutkiewicz, M.J., Wilson, J.C. and Bindschadler, R.A. (1992). Application of image cross-correlation to the measurement of glacier velocity using satellite image data. *Remote sensing of environment*, *42*(3), 177-186.

Scambos, T. A., Fahnestock, M., Moon, T., Gardner, A., and Klinger, M. (2019). Ice Speed of Antarctica (LISA), Version 1. [2016-2017]. Retrieved from http://385doi.org/10.7265/nxpce997.

Shreve, R.L. (1972). Movement of water in glaciers. *Journal of Glaciology*, *11*(62), 205-214.

Smith, B.E., Fricker, H.A., Joughin, I.R. and Tulaczyk, S. (2009). An inventory of active subglacial lakes in Antarctica detected by ICESat (2003–2008). *Journal of Glaciology*, *55*(192), 573-595.

Stearns, L.A., Smith, B.E., and Hamilton, G.S. (2008). Increased flow speed on a large East Antarctic outlet glacier caused by subglacial floods. *Nature Geoscience*, *1*(12), 827-831.

Stearns, L.A. (2007). Outlet glacier dynamics in east Greenland and East Antarctica.

Tinto, K. J., Padman, L., Siddoway, C. S., Springer, S. R., Fricker, H. A., Das, I., Caratori Tontini, F., Porter, D. F., Frearson, N. P., Howard, S. L., Siegfried, M. R., Mosbeux, C., Becker, M. K., Bertinato, C., Boghosian, A., Brady, N., Burton, B. L., Chu, W., Cordero, S. I., Dhakal, T., Dong, L., Gustafson, C. D., Keeshin, S., Locke, C., Lockett, A., O'Brien, G., Spergel, J. J., Starke, S. E., Tankersley, M., Wearing, M.G., and Bell, R. E. (2019). Ross Ice Shelf response to climate driven by the tectonic imprint on seafloor bathymetry. *Nature Geoscience*, *12*(6), 441-449.

Van der Veen, C. J. (1998). Fracture mechanics approach to penetration of bottom crevasses on glaciers. *Cold Regions Science and Technology,27*(3), 213-223.

Van Der Veen, C. J., and Whillans, I. M. (1989). Force budget: I. Theory and numerical methods. *Journal of Glaciology*, *35*(119), 53-60.

Van der Veen, C. J. (2013). *Fundamentals of glacier dynamics*. CRC press. 223

Van der Veen, C. J., Stearns, L. A., Johnson, J. T., and Csatho, B. M. (2014). Flow dynamics of Byrd Glacier, East Antarctica. *Journal of Glaciology,60*(224), 1053-1064.